

PAPER

Harmonic-balance circuit analysis for electro-neural interfaces

To cite this article: Zhijie Charles Chen *et al* 2020 *J. Neural Eng.* **17** 035001

View the [article online](#) for updates and enhancements.



The Department of Bioengineering at the University of Pittsburgh Swanson School of Engineering invites applications from accomplished individuals with a PhD or equivalent degree in bioengineering, biomedical engineering, or closely related disciplines for an open-rank, tenured/tenure-stream faculty position. We wish to recruit an individual with strong research accomplishments in Translational Bioengineering (i.e., leveraging basic science and engineering knowledge to develop innovative, translatable solutions impacting clinical practice and healthcare), with preference given to research focus on neuro-technologies, imaging, cardiovascular devices, and biomimetic and biorobotic design. It is expected that this individual will complement our current strengths in biomechanics, bioimaging, molecular, cellular, and systems engineering, medical product engineering, neural engineering, and tissue engineering and regenerative medicine. In addition, candidates must be committed to contributing to high quality education of a diverse student body at both the undergraduate and graduate levels.

[CLICK HERE FOR FURTHER DETAILS](#)

To ensure full consideration, applications must be received by June 30, 2019. However, applications will be reviewed as they are received. Early submission is highly encouraged.



PAPER

Harmonic-balance circuit analysis for electro-neural interfaces

RECEIVED
3 February 2020REVISED
8 April 2020ACCEPTED FOR PUBLICATION
16 April 2020PUBLISHED
28 May 2020Zhijie Charles Chen^{1,2,5} , Bing-Yi Wang^{3,2} and Daniel Palanker^{4,2} ¹ Department of Electrical Engineering, Stanford University, Stanford, CA, United States of America² Hansen Experimental Physics Laboratory, Stanford University, Stanford, CA, United States of America³ Department of Physics, Stanford University, Stanford, CA, United States of America⁴ Department of Ophthalmology, Stanford University, Stanford, CA, United States of America⁵ Author to whom any correspondence should be addressed.E-mail: zcchen@stanford.edu**Keywords:** neural stimulation, electro-neural interface, charge injection capacity, harmonic-balance analysis, electrochemical impedance spectrum, photovoltaic neural stimulation**Abstract**

Objective. Avoidance of the adverse electrochemical reactions at the electrode-electrolyte interface defines the voltage safety window and limits the charge injection capacity (CIC) of an electrode material. For an electrode that is not ideally capacitive, the CIC depends on the waveform of the stimulus. We study the modeling of the charge injection dynamics to optimize the waveforms for efficient neural stimulation within the electrochemical safety limits. *Approach.* The charge injection dynamics at the electrode-electrolyte interface is typically characterized by the electrochemical impedance spectrum, and is often approximated by discrete-element circuit models. We compare the modeling of the complete circuit, including a non-linear driver such as a photodiode, based on the harmonic-balance (HB) analysis with the analysis based on various discrete-element approximations. To validate the modeling results, we performed experiments with iridium-oxide electrodes driven by a current source with diodes in parallel, which mimics a photovoltaic circuit. *Main results.* Application of HB analysis based on a full impedance spectrum eliminates the complication of finding the discrete-element circuit model in traditional approaches. HB-based results agree with the experimental data better than the discrete-element circuit. HB technique can be applied not only to demonstrate the circuit response to periodic stimulation, but also to describe the initial transient behavior when a burst waveform is applied. *Significance.* HB-based circuit analysis accurately describes the dynamics of electrode-electrolyte interfaces and driving circuits for all pulsing schemes. This allows optimizing the stimulus waveform to maximize the CIC, based on the impedance spectrum alone.

1. Introduction

Electrical stimulation of neurons requires injection of a sufficient amount of charge through the electrode-electrolyte interface. The stimulation threshold depends on various factors, including the electrode geometry [1, 2], proximity to the neurons [3, 4], the pulse waveform [2, 5], the pulse duration [6, 7], and the repetition rate [2, 8]. When too much charge is injected, the potential drop across the electrode-electrolyte interface would rise beyond the safety window, enabling adverse electrochemical reactions, such as water electrolysis, which may result in damage to the electrode material and biological tissues. The charge injection capacity (CIC) of an electrode is

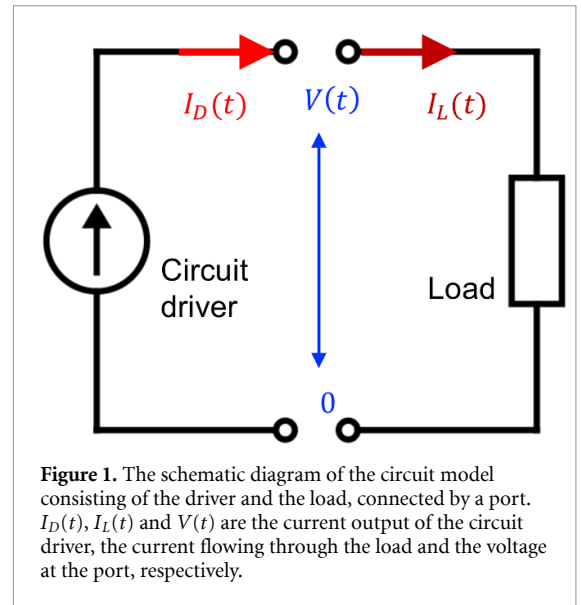
defined as the maximum amount of charge that can be injected in one pulse without driving the electrode-electrolyte interface beyond the safety window [9]. For the efficacy of neural stimulation, bio-compatible electrode materials with large CIC are desirable. Iridium oxides (IrOx) [10–15], platinum black (Pt-Black) [16] and poly(3,4-ethylene-dioxythiophene)-poly(styrenesulfonate) (PEDOT:PSS) [8, 17–19] are some common materials used as neural electrodes for this reason.

The CIC is related to the material capacitance and is affected by the impedance spectrum over a frequency range corresponding to the applied stimulus waveform [12, 20]. Very often, however, the impedance is reported only at one specific frequency,

1 kHz, for example [21], or even not reported at all [8, 14, 15, 18, 19]. Since highly capacitive materials are usually porous and often involve reversible electrochemical reactions, the electro-electrolyte interface is not ideally capacitive. Therefore, dynamics of the charge injection and the CIC depend on the applied waveform. For example, the impedance spectrum of sputtered iridium oxide film (SIROF) shows phase characteristics of the transmission lines, due to the pore resistance and the mass-transfer limitation associated with its porous structure [12, 22]. Hence, the CIC was found to vary with pulse duration [23]. Therefore, materials cannot be characterized by a single CIC value, but should rather be described in a more comprehensive manner, taking into account the impedance spectrum and the waveform of stimulus.

Traditionally, electrode-electrolyte interfaces are described by circuit models with discrete elements, the values of which are fit to the impedance spectrum. Solving the differential equations corresponding to such circuits should describe the resulting charge injection dynamics [24–26]. However, as we will show in section 3.2, depending on the applied waveform, various discrete-element approximations to the impedance spectrum may result in highly variable outcomes. An accurate representation of the impedance spectrum typically involves constant phase elements (CPEs) [27], the dynamics of which needs to be modeled in frequency domain through the Laplace transform [28], causing extra complications and often incompatible with non-linear circuit elements, such as diodes, for example.

In this paper, we propose a framework to describe the circuit response without the need to fit an equivalent discrete-element circuit model. If the circuit is driven by controlled current or voltage, directly applying the impedance spectrum in frequency domain yields the corresponding voltage or current response. In cases where neither current nor voltage is directly controlled, we use harmonic-balance (HB) analysis to solve for the response when the circuit driver is non-linear. For example, photovoltaic retinal prosthesis is driven by photodiodes, which have non-linear relationship between the voltage and the current [11]. The results of our modeling are validated by comparing with the actual experimental measurements and with the time-domain solutions of the discrete-element circuit approximation. Since the wireless photovoltaic prosthesis is inaccessible to direct measurements *in vivo*, we developed an experimental technique to mimic the prosthetic circuit without using light. The proposed framework offers a powerful tool for optimizing the design of electro-neural interfaces in general, and predicts, among other useful metrics, the CIC under any stimulation waveform for any electrode material.



2. Methods

2.1. Circuit modeling

The circuit for neural stimulation generally consists of two parts: the circuit driver and the load, as shown in figure 1. The circuit driver is a controlled power source, while the load comprises an electrochemical cell and other power consuming circuit components. These two parts are connected at a port. The output current of the circuit driver is a function of time t , denoted by $I_D(t)$. Similarly, $I_L(t)$ represents the current flowing through the load, and $V(t)$ the voltage at the port. The polarities of I_D , I_L and V are defined as in figure 1. By Kirchhoff's laws, for all t , we have

$$I_D(t) = I_L(t). \quad (1)$$

The load is typically a lumped circuit, which we assume to be linear. By the Butler-Volmer model, an electrochemical cell can be linearized within a relatively small window of overpotential, and the non-linear Tafel behavior outside this window is associated with high rate of Faradaic reactions [29], which usually should be avoided in neural stimulation. Furthermore, electrochemical impedance spectroscopy (EIS) is only meaningful for electrode-electrolyte interfaces with linear circuit behavior, and as a result, most discrete-element circuits used to model neural electrodes assume linearity. The circuit driver, however, may have non-linear current-voltage ($i-v$) relationship, especially when neither the current nor the voltage output of the circuit driver is directly controlled. For example, for photovoltaic retinal prosthesis, only the light intensity projected onto the photodiodes is directly controlled, and the $i-v$ relationship of the photodiodes is exponential [24].

2.1.1. Directly controlled driver of current or voltage

For a circuit driven by controlled $I_D(t)$ or $V(t)$, we can calculate the steady-state response of the load to

periodic stimulus directly from the impedance spectrum. Let impedance $Z(\omega) : \mathbb{R} \mapsto \mathbb{C}$, as a function of frequency ω , be the impedance spectrum of the load, and \mathcal{F} be the Fourier transform. I_D , equivalently, I_L , and V are related by

$$I_D = \mathcal{F}^{-1}[(\mathcal{F}V)/Z] = \mathbf{S}V. \quad (2)$$

(2) is a linear transform from function V to function I_D , which we denote with the linear operator \mathbf{S} . Since the impedance is typically nonzero and finite, \mathbf{S} is invertible. Therefore, given a stimulus waveform $I_D(t)$ or $V(t)$, we can calculate the corresponding response of $V(t)$ or $I_L(t)$. [28] proposes a similar approach to study the responses of electrochemical cells in frequency domain, but this method still involves equivalent circuits to calculate the Laplace transform for transient behavior. Our approach avoids the complication of finding an equivalent circuit, and can also be applied to describe the transient behaviour in the non-periodic stimulus, as shown in section 2.1.3. Note that the DC impedance $Z(0)$ is not measured in the standard EIS, and can be determined separately via chronoamperometry or methods alike. However, in neural stimulation, charge should be balanced, and therefore the DC current should be zero.

2.1.2. Nonlinear circuit driver

When neither $I_D(t)$ nor $V(t)$ is directly controlled, we can rely on the $i-v$ relationship G of the driver at each time step:

$$I_D(t) = G(V(t), t). \quad (3)$$

To vary the current, the $i-v$ relationship of the circuit driver must change with time, and hence G is a function of both V and t , which may be non-linear, such as the $i-v$ curve of a photodiode illuminated by a pulsed laser. An example of such G is given in section 2.2.1. Knowing G , we can study the steady-state response following the principles of HB analysis - comparing the current responses of the linear and the non-linear parts of the circuit, and numerically minimizing the difference between the two responses [30, 31]. The solution is found if and only if the two responses match exactly, which is required by Kirchhoff's current law (KCL). Kirchhoff's voltage law (KVL) is hardwired in the definition of V .

Today, the Newton-Raphson method is the most common approach in HB analysis [30, 31] but its implementation requires proprietary software or custom coding. Since the HB problem can be formulated as an optimization, any optimization method can be used to match the responses. To demonstrate the ease of implementation, we use an off-the-shelf optimization tool in MATLAB to find the solution. Our demonstration code is available online at [32].

For any given $V(t)$, the nominal $\tilde{I}_L(t)$ is given by (2):

$$\tilde{I}_L = \mathbf{S}V, \quad (4)$$

and the nominal $\tilde{I}_D(t)$ is given by (3). Note that $\tilde{I}_L(t)$ and $\tilde{I}_D(t)$ have no physical meanings, because generally $\tilde{I}_L(t) \neq \tilde{I}_D(t)$, which violates (1). We can define the difference between \tilde{I}_L and \tilde{I}_D as an operator acting on V :

$$\mathbf{Q}V := \mathbf{S}V - G(V, t). \quad (5)$$

The true voltage response at the port, V^* , is obtained if and only if $\|\mathbf{Q}V^*\|^2 = 0$. We perform optimization on $\|\mathbf{Q}V\|^2$ to find V^* :

$$V^* = \arg \min_V \|\mathbf{Q}V\|^2. \quad (6)$$

We prove in the Appendix that $\min_V \|\mathbf{Q}V\|^2 = 0$ and the solution $V^*(t)$ is unique, if $G(V)$ is monotonically non-increasing. The monotonicity is a realistic premise, because higher voltage at the port counteracts the current output.

2.1.3. Transient behavior

HB analysis only provides the steady-state solution of circuits under periodic stimuli [30, 31]. However, the several initial pulses may show transient behavior uncaptured in the steady-state solution, especially when they are monophasic capacitor-coupled. For example, in [24], the initial pulses are not charge-balanced, and the response to them is quite different from the steady state.

The general approach to study the transient behavior of an electrode-electrolyte interface is using the Laplace transform without assuming periodicity, which involves finding its equivalent circuit [28]. Here, we convert the transient behavior into a virtually periodic one by padding the waveform with an additional discharging phase and a checking phase. To calculate the initial pulses between $t=0$ and $t=T_0$, we insert a discharging phase of length $T_1 - T_0$ after T_0 and a checking phase of length $T_2 - T_1$ after T_1 , as illustrated in figure 2.

In the discharging phase, we keep $V(t)$ constant at the resting voltage V_0 of the load, and allow any amount of current to flow through the driver. In the checking phase, the circuit driver has the resting $i-v$ relationship $G_0(V)$ to verify the load has sufficiently discharged. The circuit driver is resting before the current injection begins, during which its $i-v$ relationship G does not change with time, and we define $G_0(V)$ as $G(V, t)$ before all stimulations. Hence, G_0 is a function of only V but not t . For the circuit driver, we have

$$\tilde{I}_D(t) = \begin{cases} G(V(t), t), & \text{if } 0 \leq t < T_0, \\ \tilde{I}_L(t), & \text{if } T_0 \leq t < T_1, \\ G_0(V(t)), & \text{if } T_1 \leq t < T_2. \end{cases} \quad (7)$$

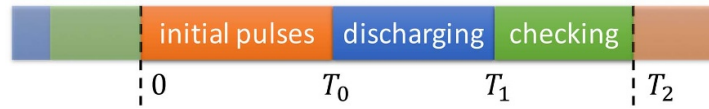


Figure 2. Schematic diagram of the augmented period consisting of the initial pulses, the discharging phase and the checking phase.

For this scheme to work properly, $T_1 - T_0$ should be at least several times longer than the time constants of the electrode relaxation and charge redistribution calculated in [33]. To verify the efficacy of the discharging phase, the deviation of $V(t)$ from V_0 in the checking phase should be negligible compared to its average magnitude between 0 and T_0 :

$$\max_{t \in [T_1, T_2]} |V(t) - V_0| \ll \overline{|V(t) - V_0|} \Big|_{t \in [0, T_0]}. \quad (8)$$

2.2. Experimental validation

2.2.1. Circuit driver

The circuit of a photovoltaic retinal prosthesis described in [11] can be driven by shining light on photodiodes. However, quantitative analysis of such circuit requires precise measurement of the irradiant power on each photodiode and their light-to-current conversion. To simplify such experiments, we use a current source in parallel with the same photodiode in the dark, which exhibits an identical $i-v$ curve, and therefore allows driving the circuit in an equivalent way as using light.

By equation (1) of [24], I_D , the output current of the photodiode, equals the short-circuit photocurrent I_{photon} minus the forward current of the diode in dark under the output voltage V :

$$I_D(V) = I_{\text{photon}} - I_{\text{forward}}(V), \quad (9)$$

and $I_{\text{forward}}(V)$ can be approximated by the exponential relationship

$$I_{\text{forward}}(V) = I_0 \left(\exp\left(\frac{Ve}{nk_B T}\right) - 1 \right), \quad (10)$$

where I_0 is the scale current, e is the elementary charge, n is the diode ideality factor, k_B is the Boltzmann constant and T is the temperature. Note that we did not explicitly use (10) to calculate I_{forward} , but rather interpolate current from measured dark $i-v$ curve of the photodiode. The dataset of the $i-v$ curve is available at [32].

By (9), the current source and the shaded photodiode D_p combined in parallel are equivalent to the photodiode in light, as shown in the red dashed box in figure 3. The ON and OFF status of the current source correspond to turning the light on and off, respectively. Because of the limited precision of the current source, we cannot set the OFF current

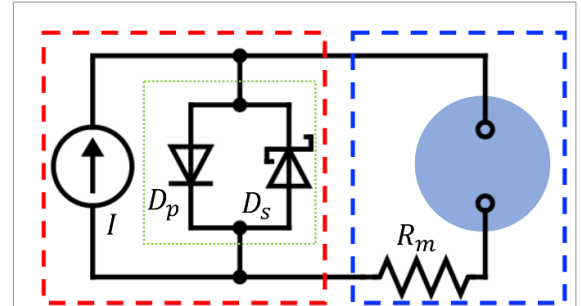


Figure 3. The circuit diagram of the experiment, consisting of the current source, the photodiode D_p , the Schottky diode D_s , the electrochemical cell (blue circle) and the monitor resistor R_m . The circuit driver and the load are noted by the red and the blue dashed boxes, respectively.

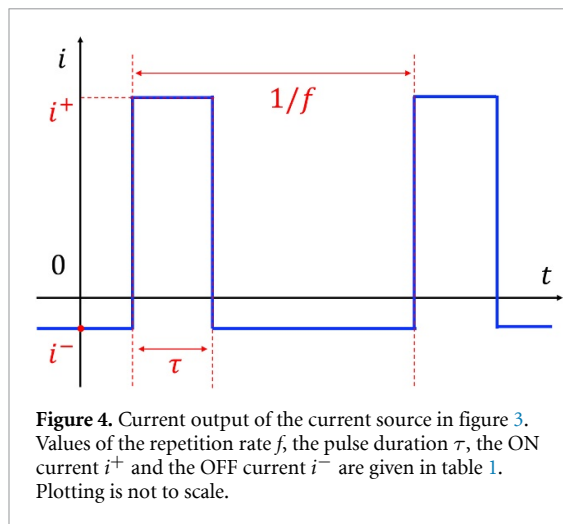
to be strictly zero between pulses. To prevent random drift of $V(t)$ due to charge accumulation, a Schottky diode D_s is connected in parallel with D_p in opposite polarity, and a negative current i^- that is much smaller in amplitude than the stimulating current i^+ is applied between pulses. In the resting state, $V \approx -0.1$ V, which is the turn-on voltage of D_s . The circuit is designed to function when $V \geq 0$, and D_s has no effect on the circuit in this range. We applied Stimulus 1 and Stimulus 2 to the current source, whose features are summarized in figure 4 and table 1. Together, the $i-v$ relationship of the circuit driver is given by

$$G(V, t) = \begin{cases} i^+ - I_{\text{forward,p}}(V), & \text{for } t \text{ during pulses } (V \geq 0), \\ i^- - I_{\text{forward,p}}(V), & \text{for } t \text{ between pulses and } V \geq 0, \\ i^- + I_{\text{forward,s}}(-V), & \text{for } t \text{ between pulses and } V \leq 0. \end{cases} \quad (11)$$

$I_{\text{forward,p}}(V)$ and $I_{\text{forward,s}}(V)$ are the $i-v$ relationship of D_p and D_s , respectively.

2.2.2. Electrochemical cell

We use an electrochemical cell of the 2-electrode setup. The working and the counter electrodes are a pair of 80 μm -diameter platinum disks coated with 400 nm of SIROF, spaced 250 μm apart center-to-center on an insulating planar substrate. The electrolyte is a cell-culture medium made of 89% of DMEM/F12 base solution, 10% of fetal



bovine serum and 1% of Penicillin ($10,000 \text{ U ml}^{-1}$)-Streptomycin (10 mg ml^{-1}) in volume. The experiment is conducted at 37°C . A resistor $R_m = 5.10 \text{ k}\Omega$ is connected in series with the electrochemical cell to monitor the current. The complete circuit is illustrated in figure 3.

To check linearity of the electrochemical cell, we first measured the impedance spectra at different voltage biases and with different perturbation amplitudes. The EIS was performed with a Gamry's Interface 1010 E potentiostat using the 2-electrode setup, with the working and counter electrodes being the pair of SIROF-coated disks mentioned above. Impedance was measured at 121 sampling frequencies (20 points per decade) between 0.1 Hz and 100 kHz. We then applied Stimulus 1 and Stimulus 2 and recorded the current (I_L) and the voltage (V) of the load. Next, we used HB analysis to calculate I_L and V directly from the impedance spectrum, and compare with the experimental measurements. For comparison, we also fit the discrete-element circuit models to the impedance spectrum and solve the corresponding differential equations for I_L and V in time domain.

3. Results

3.1. Validation of linearity by EIS

To validate that the electrochemical cell can be treated as a linear system, we performed EIS at 10 different voltage biases, evenly spaced by 0.1 V from -0.2 V to 0.7 V , with perturbation of 10 mV root-mean-square (RMS). We also measured the impedance spectrum at 0.3 V bias with 100 mV-RMS perturbation. All the spectra, plotted in figure 5(a), match each other very well, confirming linearity of the electrochemical cell. The DC impedance $Z(0)$ is determined to be $962 \text{ M}\Omega$ by chronoamperometry.

3.2. Discrete-element circuit models

A widely used equivalent circuit model of the electrode-electrolyte interface, the Randles circuit, typically includes the constant phase elements (CPEs)

Table 1. Parameters of the periodic waveform output by the current source. f , τ , i^+ and i^- are defined in figure 4.

	f (Hz)	τ (ms)	i^+ (μA)	i^- (nA)
Stimulus 1	2	50	2.679	-51.2
Stimulus 2	30	10	9.72	-255.7

Table 2. Fit values of the discrete components from the impedance spectrum.

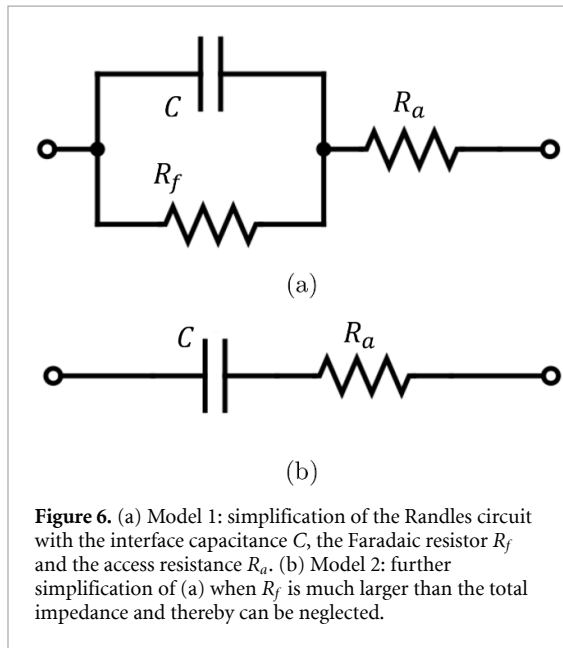
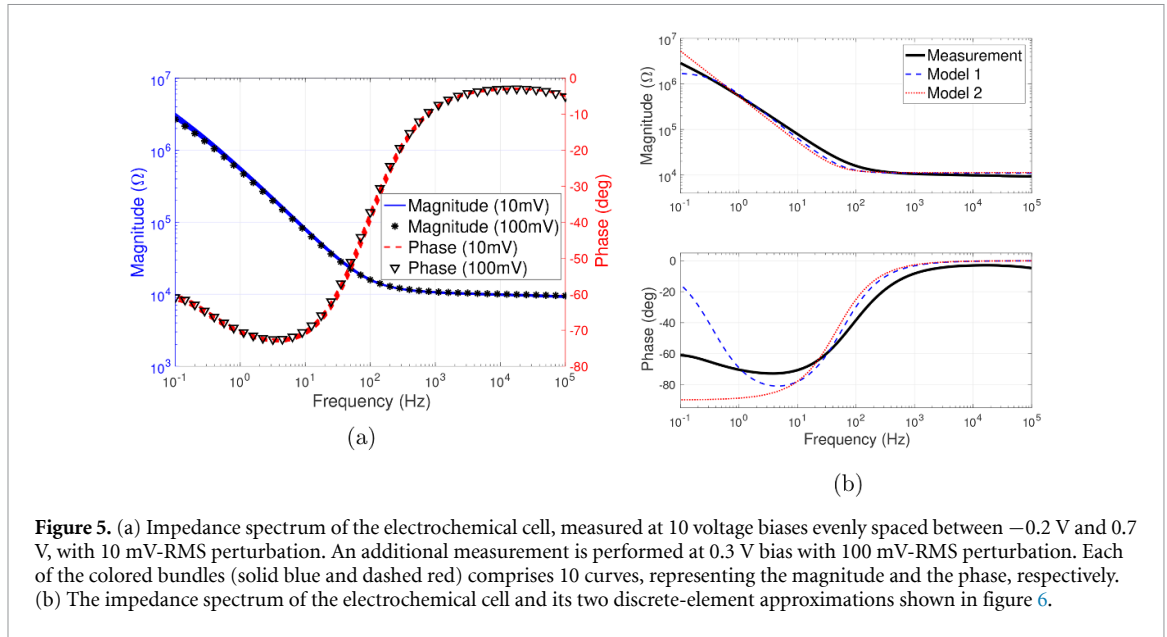
	R_a (k Ω)	R_f (M Ω)	C (nF)
Model 1	11.00	1.746	252.7
Model 2	11.30	$+\infty$	302.7

[29], the dynamics of which is given in frequency domain. However, since modeling involving a non-linear circuit driver is more convenient in time domain, a simplification of the Randles circuit, comprising only capacitors and resistors [24, 25, 34] is usually applied. Figure 6(a) shows one possible simplification consisting of the interface capacitor C , the Faradaic resistor R_f and the access resistor R_a (Model 1). Sometimes, R_f is neglected and the circuit further simplifies as illustrated in figure 6(b) (Model 2) [26]. Generally, we need two sets of lumped circuits to model the working and the counter electrodes, respectively. However, since we use symmetric working and counter electrodes, only one set of the circuit is needed in each model. We averaged all the 10 mV-RMS impedance spectra in figure 5(a), and fit the two circuit models to the mean spectrum using the method of least squares on the relative error, which is described in section 3.3.2.3 of [27]. The spectra of the fit circuits are plotted in figure 5(b), and the values of the discrete elements are shown in table 2.

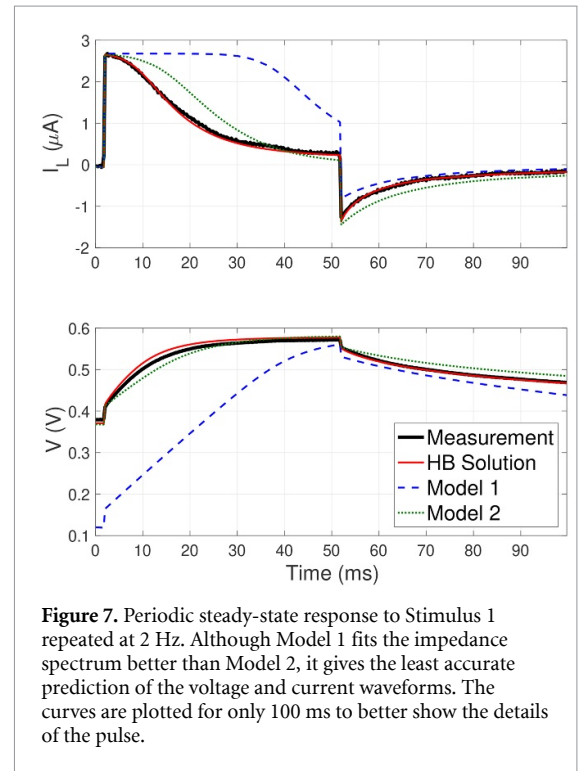
The periodic steady-state response to Stimulus 1 with Model 1 and Model 2 can be calculated by solving the differential equations in time domain using Mathematica 11. As shown in figure 7, the two models produce very different results. Since Model 2 is a special case of Model 1 where R_f is constrained at ∞ , Model 1 fits the impedance spectrum better than Model 2. However, the response calculated with Model 2 is more accurate than that with Model 1.

3.3. HB analysis for steady-state response to periodic stimulus

To find the steady-state circuit response to a periodic stimulus, we implement the optimization in (6) with the built-in non-linear least square solver (lsqnonlin) in MATLAB (R2017a). As shown in figure 7, the steady-state response to Stimulus 1 matches the experimental result better than both models in section 3.2. The response is calculated in 0.25 ms steps, yielding 2000 sampling points per period of 500 ms.



Stimulus 2 is repeated at a higher frequency of 30 Hz. Measurement and modeling were performed with another working electrode of the same geometry and material, whose impedance spectrum closely resembles that of the electrode used for Stimulus 1. We calculated the periodic steady-state response to Stimulus 2 in $50 \mu s$ steps (666 sampling points per period of 33.3 ms). The optimization converges in eight iterations for both stimuli. Figure 8 depicts the final result plotted with the starting values of $V(t)$ and $I_L(t)$, and the two intermediate iterations of the optimization. For comparison, we also calculated the response of Model 1 to Stimulus 2 using the time-domain method in section 3.2, as shown in figure 8. The time-domain solution is significantly improved at higher stimulation frequencies (Stimulus 2, 30 Hz) compared with lower frequencies (Stimulus 1, 2 Hz),



because the impedance spectrum of Model 1 fits the EIS measurement better in frequency range higher than approximately 30 Hz, although the HB solution still matches the measurement better.

3.4. HB analysis for transient behavior

Following the scheme outlined in section 2.1.3, we model the first 115 ms of the response to Stimulus 2, which includes the four initial pulses. According to figure 5 in [33], the relaxation time for SIROF electrodes of the same geometry is around 10 ms. Therefore, we design the discharging and the checking

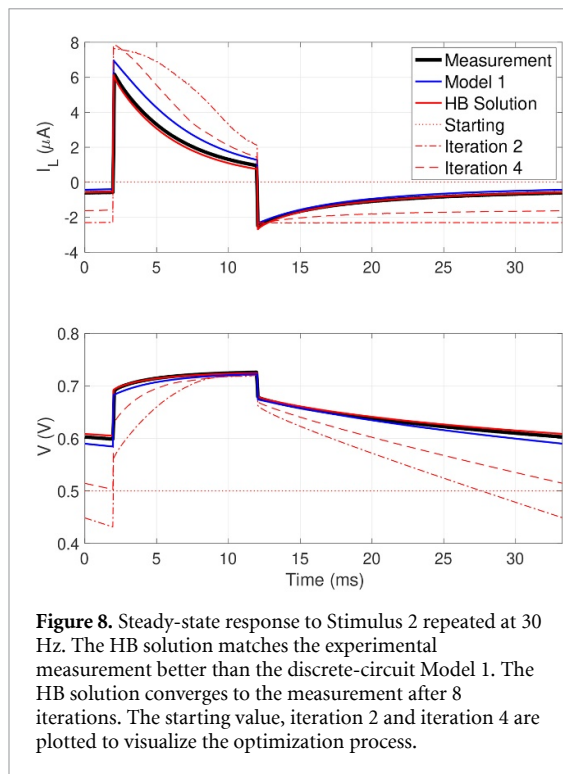


Figure 8. Steady-state response to Stimulus 2 repeated at 50 Hz. The HB solution matches the experimental measurement better than the discrete-circuit Model 1. The HB solution converges to the measurement after 8 iterations. The starting value, iteration 2 and iteration 4 are plotted to visualize the optimization process.

phases to be 60 ms and 15 ms, respectively. The transient response based on HB analysis, calculated in 50 μ s steps (3800 sampling points per augmented period of 190 ms) with convergence after 10 iterations, is plotted in figure 9, and it matches the experimental measurement well. The last pulse in this sequence is already fairly close to the periodic steady-state response to Stimulus 2, shown in figure 8.

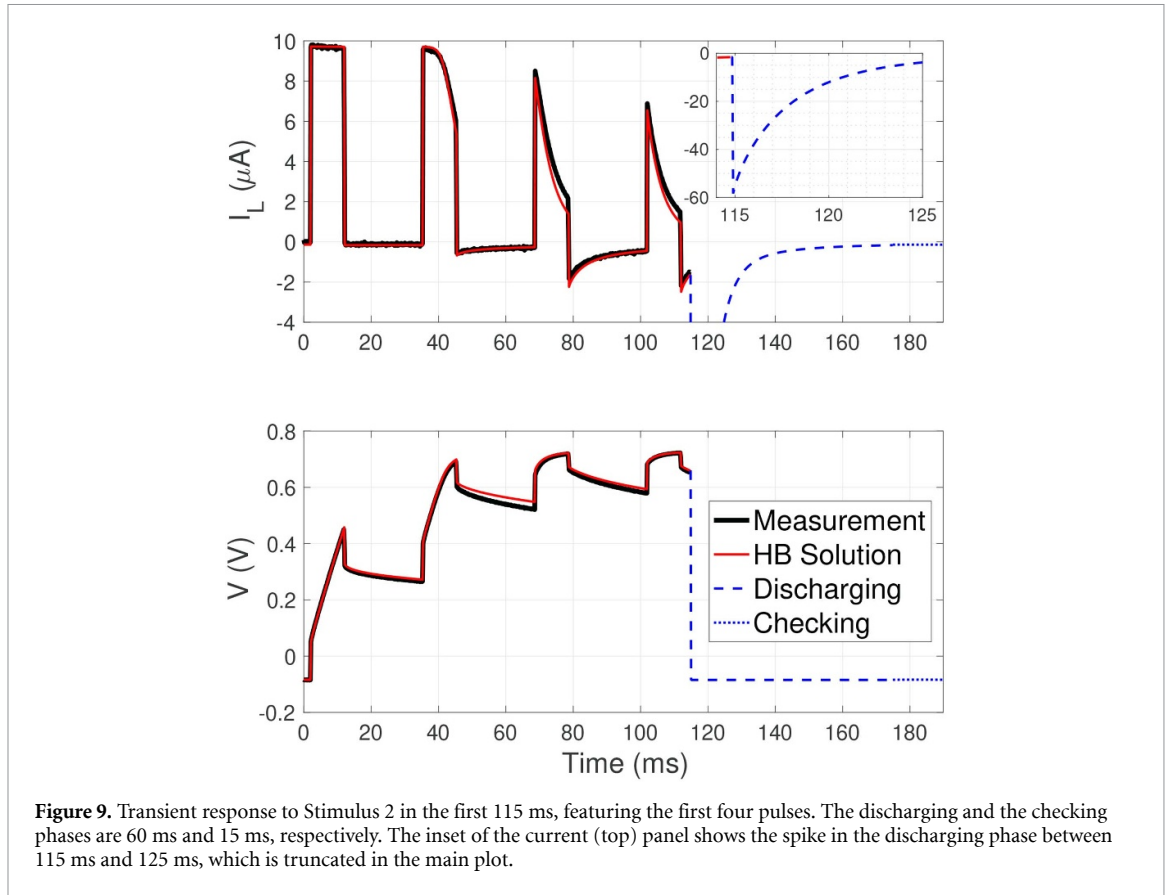
4. Discussion

Successful design of electro-neural interfaces requires comprehensive understanding of the electrode response to given current or voltage stimuli. Only under the assumption that the electrode is ideally polarizable could the electrode-electrolyte interface be treated as a simple capacitor and CIC has a fixed value. In reality, an electrode material usually exhibits more complex impedance spectrum than what can be represented by a simple RC series. One reason for this complexity is that materials capable of storing large amount of charge usually have porous surfaces [20], and some even allow diffusion into the bulk of the electrode [27]. Dynamics of the charge transfer to distributed double layer or redox sites leads to a phase element characteristic of a transmission line in the impedance spectrum [12, 22, 27, 29], and therefore, the CIC becomes waveform-specific. Hence, a computational framework for proper modeling of the electrode-electrolyte interface is nontrivial and important.

One way to model the electrode response is by fitting a discrete-circuit model, comprising capacitors

and resistors, to the impedance spectrum, and solving the differential equations in time domain. However, we have demonstrated that the solutions are highly susceptible to small variations in the discrete-element approximations widely used in engineering of electro-neural interfaces. Figure 5(b) shows that both discrete-element models approximate the impedance spectrum well in most of the frequency range, except for the low-frequency end. Model 1 includes the Faradaic resistor to improve the fitting, but the self-discharge of the electrodes between pulses is overestimated as a result. Calculation of the response to Stimulus 1 repeated at 2 Hz with Model 1 shows much higher CIC than in reality. Model 2 does not capture the electrode discharge mechanism, but predicts the response better, even though it approximates the spectrum worse than Model 1. The effect of the Faradaic resistor is so prominent because the stimulation period is comparable to the RC time constant of the self-discharge loop (R_f and C). Although the specific discrete-circuit model predicts the response better with stimuli repeated at higher frequency (30 Hz), this itself illustrates the problem that a match between the discrete-element circuit model and experiment varies with the stimulus shape. With more resistors and capacitors, one can build models that better approximate the full spectrum using phasor analysis [35]. A more accurate approximation usually requires CPEs [12, 27–29], and there are established tools to generate discrete-element models for different physical processes that induce the CPEs, which typically takes 1 to 1.5 circuit lumps per frequency decade to yield a good fit [36]. However, rather than incrementally improving the accuracy of the approximation, a better approach is to directly apply the impedance spectrum without any approximations. Even though the equivalent circuit models are useful for mechanistic description of various processes in electrochemistry, they may not be the most efficient approach for electro-neural engineering.

Some electro-neural interfaces are driven by non-linear power sources, such as photodiodes [11] or phototransistors [15]. The proposed HB technique enables computational analysis of circuits with non-linear elements. By minimizing the difference between the responses of the linear load and the non-linear circuit driver, the true solution is found if and only if the difference vanishes. HB analysis is adopted because of the convenience to incorporate distributed components described in frequency domain [30]. We show that if the circuit driver has a non-increasing $i-v$ relationship, the optimization is guaranteed to converge to the unique true solution. Note that our separation of the circuit into the driver and the load is nominal, only for the convenience of discussion. If the load has non-linear components, it can be lumped with the non-linear part of the circuit driver to keep the nominal load linear.



The efficient optimization-based HB technique is enabled by advances in optimization research and the growing power of computers. Many optimization algorithms are shown to converge linearly (the distance to the solution decreases exponentially with the number of iterations, i.e. $\|\epsilon_{n+1}\| \leq \beta \|\epsilon_n\|$, where ϵ_n is the distance to the true solution after the n^{th} iteration and β is a constant such that $0 < \beta < 1$), some even quadratically ($\|\epsilon_{n+1}\| \leq \beta \|\epsilon_n\|^2$) [37]. Modeling the electro-electrolyte interfaces is a small-scale problem compared with typical applications of HB analysis in radio-frequency circuit design, so an off-the-shelf optimization tool can solve the system efficiently. The runtime of the optimization varies from a few seconds (Stimulus 2, 666 sampling points) to about a minute (the transient modeling, 3800 sampling points) on a laptop computer (3.1 GHz dual-core CPU, 8 GB of memory). We demonstrated the baseline capability of HB analysis using a simple implementation, and the computational efficiency can be further improved with more sophisticated algorithms. For example, modern HB software uses the Newton-Raphson method, which is a powerful algorithm for finding zeros of non-linear multivariate functions [31]. In addition, a variety of highly efficient algorithms are developed for convex optimization [38], although the specific optimization in (6) is not convex. The comparison of different numerical methods is beyond the scope of this paper.

Standard HB analysis can only be applied to periodic waveforms, i.e. it assumes a steady state when repetitive pulsing is applied [30, 31]. We adapted the HB technique to model the transient behavior in the beginning of a long burst of pulses by virtually augmenting the period with the discharging and the checking phases. This adaptation is possible when the electrode-electrolyte interface takes only several cycles before it reaches the steady state, as is the case of typical neural stimulation settings. We demonstrated that the computational workload of the optimization is manageable on a laptop computer, if the number of sampling points in a period is on the order of a few thousands. If the ramp-up would include hundreds or thousands of cycles, as in typical radio-frequency circuits, our adaptation would be computationally inefficient. It also would be inefficient if the pulse duration is very short compared to the period since most sampling points would fall in the inter-pulse intervals the details of which are not of particular interest. Similarly, our adaptation is not applicable to the case when the discharge time of the electrode is much longer than the transient behavior.

We developed an experimental technique that enables testing the characteristics of photovoltaic electro-neural interfaces without using light. The observation that a current source and a shaded photodiode in parallel mimic the $i-v$ relationship of the illuminated photodiode greatly simplifies the experiments, which would otherwise require optical setup

with precise measurements of the irradiant power on the diode and the light-to-current conversion efficiency.

The framework we proposed requires the electrode-electrolyte interface to be linear within the relevant voltage range. Linearity is also the underlying premise of using EIS to characterize the electrode. We verified the linearity on SIROF electrodes by performing the EIS at different voltage biases (-0.2 V to 0.7 V) and different perturbation amplitudes (10 mV and 100 mV). To avoid excessive Faradaic reactions in neural stimulation, the electrochemical overpotential is usually limited to a relatively small range, where the electrode-electrolyte interface exhibits linear behavior.

For neural stimulation, even if electrodes are in close contact with tissue, vast majority of electric current flows through the extracellular medium between the electrode and the neurons rather than through the cell membrane, as evidenced by much lower seal resistance (≈ 50 M Ω) than the membrane resistance (≈ 20 G Ω) [39]. Therefore, changes in the cell membrane conductivity due to opening and closing of the voltage-gated ion channels are unlikely to significantly affect the tissue impedance. However, at the onset of stimulation, biological tissue may also respond by gradual changes of its impedance due to change in the metabolic activity, which may affect the osmotic balance, affecting cellular volume, shape and hence the tissue impedance. In extreme stimulation conditions, exceeding the safety limits, tissue might be damaged by electroporation or pH changes, and hence will change its impedance very significantly. Nevertheless, under safe chronic stimulation, tissue properties are expected to be stable and hence maintain linearity of the electrode-electrolyte interface.

In the future, this computational method could be extended to cover the case when the impedance spectrum is piece-wise linear, for example, corresponding to different Faradaic reactions within different voltage ranges.

5. Conclusions

We established a computational framework to study electro-neural interfaces and the associated electrical circuit dynamics. To model the steady state under periodic stimulus, we directly apply the impedance spectrum to the stimulus in frequency domain. If non-linear components are involved, we implement HB analysis using a rapidly converging optimization. By adding the discharging and the checking phases in a period, the HB technique is also adapted to study the transient behavior in the beginning of a burst of pulses. We demonstrate that the HB optimization is computationally tractable on a laptop computer, and guaranteed to converge to a unique solution if the circuit driver has a non-increasing $i-v$

relationship. Comparing the computational results to the experimental measurements, we show superiority of the HB method over the discrete-element circuit approximations.

Acknowledgment

The authors would like to thank Professor Lenya Ryzhik from Department of Mathematics at Stanford University, Professor Boris Murmann, Dr Dante Muratore and Stephen Weinreich from Department of Electrical Engineering at Stanford University, Dr Ken Kundert from Designer's Guide Consulting, Inc. and Professor Stuart Cogan and Atefeh Ghazavi from Department of Bioengineering at the University of Texas at Dallas for the very helpful discussions. Funding was provided by the National Institutes of Health (Grants No. R01-EY-018608 and No. R01-EY-027786), the Stanford Neurosciences Institute, and Research to Prevent Blindness.

Appendix

Here we show the existence of a unique solution V^* to the optimization (6), such that

$$\|\mathbf{QV}^*\|^2 = 0, \quad (\text{A1})$$

if $\|\mathbf{QV}\| \rightarrow +\infty$ when $\|V\| \rightarrow +\infty$, and $G(V, t)$ is monotonically non-increasing in V for all t .

Proof. First, we show the existence of such V^* , by proving

$$\min_V \|\mathbf{QV}\|^2 = 0. \quad (\text{A2})$$

Because $\|\mathbf{QV}\| \rightarrow +\infty$ when $\|V\| \rightarrow +\infty$ and $\|\mathbf{QV}\|^2 \geq 0$, $\|\mathbf{QV}\|^2$ has a minimum. We now show that all extrema of $\|\mathbf{QV}\|^2$ are 0. Suppose $\|\mathbf{QV}\|^2$ is an extremum at V_0 . By the Karush-Kuhn-Tucker conditions,

$$\langle \mathbf{Q}[V_0] | \delta \mathbf{Q} \rangle = \langle \mathbf{Q}[V_0] | \int \frac{\delta \mathbf{Q}[V_0]}{\delta V}(t) \delta V(t) dt \rangle = 0 \quad (\text{A3})$$

for any variational δV . By equation (5),

$$\int \frac{\delta \mathbf{Q}[V_0]}{\delta V}(t) \delta V(t) dt = \left(\mathbf{s} - \frac{\partial G}{\partial V} \right) \delta V. \quad (\text{A4})$$

Therefore, we have

$$\langle \mathbf{Q}[V_0] | \left(\mathbf{s} - \frac{\partial G}{\partial V} \right) \mathbf{Q}[V_0] \rangle = 0. \quad (\text{A5})$$

The net power consumption of the load is positive, so by definition, for all $V \neq 0$, $\langle V | \mathbf{S} V \rangle > 0$. Because $\frac{\partial G}{\partial V}$ is non-positive, we also have:

$$\langle V | \left(\mathbf{s} - \frac{\partial G}{\partial V} \right) V \rangle > 0, \quad (\text{A6})$$

for all $V \neq 0$, which implies

$$\mathbf{Q}[V_0] = 0. \quad (\text{A7})$$

Therefore, $\|\mathbf{Q}V\|^2$ has at least one minimum at V_0 , and all extrema of $\|\mathbf{Q}V\|^2$, including V_0 , are 0.

Next, we show the uniqueness of the minimum. We prove, by contradiction, a stronger claim that $\mathbf{Q}V$ is injective, from which the uniqueness directly results. Assume there exist V_1 and V_2 , such that $\mathbf{Q}[V_1] = \mathbf{Q}[V_2]$ but $V_1 \neq V_2$. We define a function $P: [0, 1] \rightarrow \mathbb{R}$ by

$$P(x) := \langle V_1 - V_2 | \mathbf{Q}[xV_1 + (1-x)V_2] \rangle. \quad (\text{A8})$$

By (A6), we have:

$$\begin{aligned} P(1) - P(0) &= \int_0^1 P'(x) dx \\ &= \int_0^1 \langle V_1 - V_2 | \left(\mathbf{S} - \frac{\partial \mathbf{G}}{\partial V} \right) (V_1 - V_2) \rangle dx > 0. \end{aligned} \quad (\text{A9})$$

However, we also have

$$\begin{aligned} P(1) &= \langle V_1 - V_2 | \mathbf{Q}[V_1] \rangle \\ &= \langle V_1 - V_2 | \mathbf{Q}[V_2] \rangle = P(0), \end{aligned} \quad (\text{A10})$$

which is a contradiction, and it follows that $\mathbf{Q}V$ is injective. Therefore, $\|\mathbf{Q}V^*\|^2 = 0$ is the unique minimum of (6). \square

ORCID iDs

Zhijie Charles Chen  <https://orcid.org/0000-0003-2705-065X>

Bing-Yi Wang  <https://orcid.org/0000-0001-8336-3285>

Daniel Palanker  <https://orcid.org/0000-0002-0480-3025>

References

- [1] Flores T et al 2019 Honeycomb-shaped electro-neural interface enables cellular-scale pixels in subretinal prosthesis *Sci. Rep.* **9** 1–12
- [2] Elton H et al 2019 Characteristics of prosthetic vision in rats with subretinal flat and pillar electrode arrays *J. Neural Eng.* **16** 066027
- [3] Flores T, Lei X, Huang T, Lorach H, Dalal R, Galambos L, Kamins T, Mathieson K and Palanker D 2018 Optimization of pillar electrodes in subretinal prosthesis for enhanced proximity to target neurons *J. Neural Eng.* **15** 036011
- [4] Rattay F, Bassereh H and Fellner A 2017 Impact of electrode position on the elicitation of sodium spikes in retinal bipolar cells *Sci. Rep.* **7** 1–12
- [5] Wang B, Petrossians A and Weiland J D 2014 Reduction of edge effect on disk electrodes by optimized current waveform *IEEE Trans. Biomed. Eng.* **61** 2254–63
- [6] Boinagrov D, Loudin J and Palanker D 2010 Strength–duration relationship for extracellular neural stimulation: numerical and analytical models *J. Neurophysiol.* **104** 2236–48
- [7] Boinagrov D, Pangratz-Fuehrer S, Goetz G and Palanker D 2014 Selectivity of direct and network-mediated stimulation of the retinal ganglion cells with epi-, sub- and intraretinal electrodes *J. Neural Eng.* **11** 026008
- [8] Ghezzi D et al 2013 A polymer optoelectronic interface restores light sensitivity in blind rat retinas *Nat. Photon.* **7** 400
- [9] Leung R T, Shivdasani M N, Nayagam D A X and Shepherd R K 2014 In vivo and in vitro comparison of the charge injection capacity of platinum macroelectrodes *IEEE Trans. Biomed. Eng.* **62** 849–57
- [10] Negi S, Bhandari R, Rieth L, van Wagenen R and Solzbacher F 2010 Neural electrode degradation from continuous electrical stimulation: comparison of sputtered and activated iridium oxide *J. Neurosci. Methods* **186** 8–17
- [11] Lorach H et al 2015 Photovoltaic restoration of sight with high visual acuity *Nat. Med.* **21** 476
- [12] Weiland J D and Anderson D J 2000 Chronic neural stimulation with thin-film, iridium oxide electrodes *IEEE Trans. Biomed. Eng.* **47** 911–18
- [13] Fan L-S 2013 Toward a high visual-acuity retinal prosthesis 2013 *Transducers and Eurosensors XXVII: The 17th Int. Conf. on Solid-State Sensors, Actuators and Microsystems (TRANSDUCERS and EUROSENSORS XXVII)* (Piscataway, NJ: IEEE) pp 738–43
- [14] Daschner R, Rothermel A, Rudorf R, Rudorf S and Stett A 2018 Functionality and performance of the subretinal implant chip alpha ams *Sens. Mater.* **30** 179–92
- [15] Damle S, Liu Y-H, Arya S, Oesch N W and Yu-Hwa L 2020 Vertically integrated photo junction-field-effect transistor pixels for retinal prosthesis *Biomedical Optics Express* **11** 55–67
- [16] Boretius T, Badia J, Pascual-Font A, Schuettler M, Navarro X, Yoshida K and Stieglitz T 2010 A transverse intrafascicular multichannel electrode (time) to interface with the peripheral nerve *Biosensors and Bioelectronics* **26** 62–9
- [17] Ferlauto L, Leccardi M J I A, Chenais Nig A L, Gilliéron S C A, Vagni P, Bevilacqua M, Wolfensberger T J, Sivula K and Ghezzi D 2018 Design and validation of a foldable and photovoltaic wide-field epiretinal prosthesis *Nat. Commun.* **9** 992
- [18] Benfenati F and Lanzani G 2018 New technologies for developing second generation retinal prostheses *Lab Animal* **47** 71
- [19] Maya-Vetencourt J F et al 2017 A fully organic retinal prosthesis restores vision in a rat model of degenerative blindness *Nat. Mater.* **16** 681
- [20] Cogan S F, Ehrlich J, Plante T D, Smirnov A, Shire D B, Gingerich M and Rizzo J F 2009 Sputtered iridium oxide films for neural stimulation electrodes *J. Biomed. Mater. Res. B* **89** 353–61
- [21] Musk E et al 2019 An integrated brain-machine interface platform with thousands of channels *J. Med. Internet Res.* **21** e16194
- [22] Cogan S F 2008 Neural stimulation and recording electrodes *Annu. Rev. Biomed. Eng.* **10** 275–309
- [23] Ghazavi A, Maeng J, Black M, Salvi S and Cogan S 2019 Electrochemical characteristics of ultramicro-dimensioned sifro electrodes for neural stimulation and recording *J. Neural Eng.* **17** 016022
- [24] Boinagrov D, Lei X, Goetz G, Kamins T I, Mathieson K, Galambos L, Harris J S and Palanker D 2015 Photovoltaic pixels for neural stimulation: circuit models and performance *IEEE Trans. Biomed. Circuits Syst.* **10** 85–97
- [25] Rand D et al 2018 Direct electrical neurostimulation with organic pigment photocapacitors *Adv. Mater.* **30** 1707292
- [26] Noorsal E, Sooksood K, Hongcheng X, Hornig R, Becker J and Ortman M 2011 A neural stimulator frontend with high-voltage compliance and programmable pulse shape for epiretinal implants *IEEE J. Solid-State Circuits* **47** 244–56
- [27] Barsoukov E and Macdonald J R 2005 *Impedance Spectroscopy: Theory, Experiment and Applications* (New York: Wiley)

- [28] Aurian-Blajeni B 1992 The numerical inversion of the laplace transform applied to impedance spectroscopy *J. Appl. Electrochem.* **22** 553–7
- [29] Bard A J and Faulkner L R 2001 *Electrochemical methods: fundamentals and applications* 2nd edn (New York: Wiley)
- [30] Kundert K S 1999 Introduction to RF simulation and its application *IEEE J. Solid-State Circuits* **34** 1298–1319
- [31] Maas S A 2003 Harmonic balance analysis and related methods *Nonlinear Microwave and RF Circuits* Ch 3 (Norwood, MA: Artech House, Inc.) pp 119–214
- [32] Chen Z C 2020 HBA demonstration for electro-neural interfaces v1.1 (https://github.com/CCCharlesChanHBA/_demo)
- [33] Chen Z, Ryzhik L and Palanker D 2020 Current distribution on capacitive electrode-electrolyte interfaces *Phys. Rev. Appl.* **13** 014004
- [34] Shah S, Hines A, Zhou D, Greenberg R J, Humayun M S and Weiland J D 2007 Electrical properties of retinal–electrode interface *J. Neural Eng.* **4** S24
- [35] Kundert K 2011 Introduction to phasors (<https://designers-guide.org/theory/phasors.pdf>) (Accessed 31 January 2020)
- [36] Kundert K 2008 The fracpole suite (<https://designers-guide.org/modeling/suite.pdf>) (Accessed 31 January 2020)
- [37] Luenberger D G and Yinyu Y 2015 *Linear and Nonlinear Programming* (Berlin: Springer) vol 228
- [38] Boyd S and Vandenberghe L 2004 *Convex Optimization* (Cambridge: Cambridge University Press)
- [39] Shmoel N, Rabieh N, Ojovan S M, Erez H, Maydan E and Spira M E 2016 Multisite electrophysiological recordings by self-assembled loose-patch-like junctions between cultured hippocampal neurons and mushroom-shaped microelectrodes *Sci. Rep.* **6** 1–11